ARTICLE   OPEN

Check for updates

Multiple quantum phase transitions of different nature in the topological kagome magnet $Co_3Sn_{2-x}In_xS_2$

Z. Guguchia [1] ✉, H. Zhou[2,3], C. N. Wang[1], J.-X. Yin [4], C. Mielke III [1,5], S. S. Tsirkin [5], I. Belopolski[4], S.-S. Zhang[4], T. A. Cochran[4], T. Neupert [5], R. Khasanov [1], A. Amato [1], S. Jia [2,3], M. Z. Hasan [4,6,7,8] and H. Luetkens [1]

The exploration of topological electronic phases that result from strong electronic correlations is a frontier in condensed matter physics. One class of systems that is currently emerging as a platform for such studies are so-called kagome magnets based on transition metals. Using muon spin-rotation, we explore magnetic correlations in the kagome magnet $Co_3Sn_{2-x}In_xS_2$ as a function of In-doping, providing putative evidence for an intriguing incommensurate helimagnetic (HM) state. Our results show that, while the undoped sample exhibits an out-of-plane ferromagnetic (FM) ground state, at 5% of In-doping the system enters a state in which FM and in-plane antiferromagnetic (AFM) phases coexist. At higher doping, a HM state emerges and becomes dominant at the critical doping level of only $x_{cr,1} \simeq 0.3$. This indicates a zero temperature first order quantum phase transition from the FM, through a mixed state, to a helical phase at $x_{cr,1}$. In addition, at $x_{cr,2} \simeq 1$, a zero temperature second order phase transition from helical to paramagnetic phase is observed, evidencing a HM quantum critical point (QCP) in the phase diagram of the topological magnet $Co_3Sn_{2-x}In_xS_2$. The observed diversity of interactions in the magnetic kagome lattice drives non-monotonous variations of the topological Hall response of this system.

INTRODUCTION

Layered systems featuring a Kagome lattice provide an ideal playground for discovering and understanding the topological electronic states in strongly correlated materials[1–14]. The crystal structure of the material $Co_3Sn_2S_2$[15–18] is layered featuring a kagome lattice of CoSn. It was shown to have an out-of plane ferromagnetic ground state (Curie temperature of $T_C \simeq 177$ K) with a magnetization arising mainly from the cobalt moments. This ferromagnetic semimetal has been shown to possess both a large anomalous Hall conductivity of $1130\,\Omega^{-1}\,cm^{-1}$[19,20] and a giant anomalous Hall angle of 20%[20–22] in the 3D bulk. Density functional theory (DFT) calculations have predicted several pairs of Weyl points located only 60 meV above the Fermi level[23]. Recently, using the combination of ARPES and μSR experiments we established $Co_3Sn_2S_2$ as a material that hosts a topological electronic structure and frustrated magnetism[6,24]. Namely, we showed that there is volume wise competition between ferromagnetic order of Co spins along the c-axis, and 120° antiferromagnetic order of Co spins within the kagome plane[6]. Moreover, we find a near-perfect correlation between the topological Hall conductivity and the ferromagnetically ordered volume fraction as a function of temperature. Theoretical modelling, considering both localized and itinerant electrons, was recently shown[11] to reproduce the out-of-plane ferromagnetism and 120° antiferromagnetic ordering in the kagome plane, as we observed experimentally[6]. Frustration in the magnetic kagome lattice was also shown to drive an exchange biased anomalous Hall effect[25]. However, despite knowing the remarkable thermodynamic response of the magnetic and topological states in $Co_3Sn_2S_2$, a possible quantum phase transition (QPT), as shown from standard magnetization measurements[19,26], is less studied, despite being crucial to get full insight into the link between magnetic and topological transitions in this system. A QPT is a transition between a quantum ordered phase and a quantum disordered phase, occuring at zero temperature as function of pressure, magnetic field, or doping and is driven by quantum rather than thermal fluctuations[27–32]. Since the bulk magnetization[19] is a very indirect probe for the magnetic structure, it is essential to explore the temperature-doping phase diagram using a microscopic magnetic probe. Namely, to study how the phase competition between the AFM state and the topological FM structure (which exhibits a strong AHC response in undoped $Co_3Sn_2S_2$) evolves as a function of In-doping. Furthermore, understanding the nature of the magnetic to paramagnetic quantum phase transition (QPT) is crucial, e.g., whether it is first-order or second-order (continuous) in nature. There is quantum criticality associated with a second-order QPT, that may cause intriguing electronic phases. In case of a first-order QPT[28–32], the system is expected to exhibit phase coexistence and abrupt changes in the ground state.

We have employed high-resolution muon spin relaxation/ rotation (μSR) and transport experiments to systematically characterize the temperature-doping phase diagram in $Co_3Sn_{2-x}In_xS_2$. μSR is extremely sensitive local magnetic probe. Namely, using μSR the magnetic volume fraction and the ordered moment size can be measured independently. Therefore it is ideally suited to distinguish between the first-order or second-order behavior at a QPT. The current results indicate that the out-of-plane FM ground state transitions into mixed (FM+AFM)-states or (FM+HM)-states 5 and 10% of In-doping, respectively (see Fig. 1).

[1]Laboratory for Muon Spin Spectroscopy, Paul Scherrer Institute, Villigen, Switzerland. [2]International Center for Quantum Materials and School of Physics, Peking University, Beijing, China. [3]CAS Center for Excellence in Topological Quantum Computation, University of Chinese Academy of Science, Beijing, China. [4]Laboratory for Topological Quantum Matter and Advanced Spectroscopy (B7), Department of Physics, Princeton University, Princeton, NJ, USA. [5]Department of Physics, University of Zürich, Zürich, Switzerland. [6]Princeton Institute for the Science and Technology of Materials, Princeton University, Princeton, NJ, USA. [7]Materials Sciences Division, Lawrence Berkeley National Laboratory, Berkeley, CA, USA. [8]Quantum Science Center, Oak Ridge, TN, USA. ✉email: zurab.guguchia@psi.ch
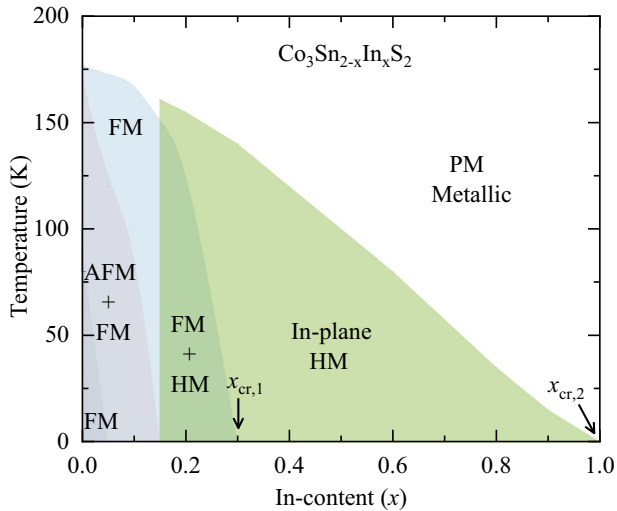
Fig. 1 (Color online) Schematic temperature-doping magnetic phase diagram of CoSn$_{2-x}$In$_x$S$_2$. FM, AFM, and HM denote the out-of-plane ferromagnetic, in-plane antiferromagnetic and in-plane helimagnetic orders, respectively (see the text for the explanation).

Finally, the putative in-plane HM state is established at the critical doping level of $x_{cr,1} \simeq 0.3$, above which the intrinsic anomalous Hall conductivity becomes negligibly small. Interestingly, the QPT between the FM and HM states is first order. In contrast, the quantum evolution of the helimagnet–paramagnet transition at zero temperature happens as a second-order transition with $x_{cr,2} \simeq 1$. These results demonstrate not only the effective In-doping tuning of the competition between FM and in-plane AFM magnetic correlations, but that the competing magnetic correlations determine the anomalous Hall response of this system. Moreover, the current results uncover the first-order QPT transition as well as an AFM quantum critical point (QCP) in the phase diagram of the kagome magnet Co$_3$Sn$_{2-x}$In$_x$S$_2$.

RESULTS

Temperature and doping dependence of microscopic magnetic response

Zero-field (ZF) μSR signals for Co$_3$Sn$_{2-x}$In$_x$S$_2$ recorded at 5 K for different indium dopant concentrations are shown in Fig. 2a. The frequency and amplitude of ZF oscillation are the measures of the ordered moment size and the magnetic volume fraction, respectively. ZF μSR spectra for Co$_3$Sn$_{2-x}$In$_x$S$_2$ reveal clear oscillations for In-doping levels $x \leq 0.9$. This points to the presence of the long-range magnetic order and a well-defined internal field, associated to it. For the $x = 1$ sample, we observe relaxation with low amplitude and with no well-defined oscillations. Longitudinal field μSR (see Supplementary Figs. 1 and 2) experiments indicate that this relaxation arises from dynamic spin fluctuations within a small fraction of the sample. The majority of the fraction shows the weak Gaussian μSR depolarization[33], evidencing the dominant paramagnetic state for $x = 1$ sample (see Supplementary Fig. 1 and the Supplementary Note 1). For $x = 1.1$, the entire sample volume shows paramagnetic response. To better visualize the effect of doping on the magnetic response, Fourier transform (FFT) amplitudes of the μSR time spectra are shown at $T = 5$ K for various In-doping (Fig. 2b), which is a measure for the the internal field distribution. For the undoped sample, the FFT amplitude recorded at 165 K is also shown. For $x = 0$ sample, a well-defined single internal field is observed with a narrow width of the field distribution in the sample, which was explained by the presence of a homogeneous out-of-plane ferromagnetic ground state[6]. However, at temperatures above $T_C^* \sim 90$ K, a second lower

internal field is observed in the μSR spectra (165 K spectrum is shown as an example), which was interpreted as the appearance of the high-temperature in-plane AFM state. It was also shown that the in-plane AFM component with a larger width of the field distribution (component II) appears above $T_C^* \sim 90$ K, causing the reduction of the volume fraction of the FM component[6]. It is interesting that for the low In-doped $x = 0.05$ and 0.1 samples, two distinct internal fields appear in the μSR spectra already at the base temperature. This suggests the presence of spatially separated antiferromagnetically and ferromagnetically ordered regions already in the ground state of the $x = 0.05$ and 0.1 samples, implying that $T_C^* \simeq 0$. But, as the temperature increases, a transition from a two-field to a single-field is observed across 100 K (see Fig. 2c) and only the high-field narrow FM component remains at high temperatures. So, the results of $x = 0.05$ and 0.1 samples show that the FM component becomes dominant and occupies the full sample volume at high temperatures, while the ground state is characterized by spatially separated FM and AFM regions. For the samples with $x \geq 0.3$, we observed the field distribution (Eq. 3) which is characterized by minimum (B_{min}) and maximum (B_{max}) cutoff fields (see Fig. 2b), which is consistent with the incommensurate helimagnetic order, observed in MnSi[34–36] and MnP[37,38]. The cutoff fields B_{min} and B_{max} are measures of the magnetic order parameter of the helimagnetic state. The difference between B_{min} and B_{max} increases with increasing In-content. For $x = 0.15$ and 0.2 samples, both the commensurate FM peak and incommensurate HM field distribution are observed simultaneously. These results show that within a narrow region of In-concentration, the magnetic ground state changes from FM to a mixed FM and AFM/HM and finally to a fully HM state.

In the following, we provide the quantitative information about the muon spin relaxation rate, the magnetic volume fraction, and the static internal field size at the muon site (data analysis procedure is described in the methods section). The temperature dependences of the internal fields ($B_{int} = \omega / \gamma_\mu^{-1}$) for the two components for $x = 0.05$ and 0.1 samples are shown in the Fig. 3a, d, respectively. Both order parameters show a monotonous decrease. Remarkably, the two components have significantly different transition temperatures, with the AFM component having an onset at $T_{AFM} \simeq 120$ K ($x = 0.05$) and 100 K ($x = 0.1$), and the FM component at $T_{FM} \simeq 175$ K ($x = 0.05$) and 170 K ($x = 0.1$). Remarkably, there is a volume-wise interplay between FM and AFM states similar to that observed in the undoped sample, since the volume fraction of the AFM component decreases with increasing temperature and above 120 and 100 K the full volume of the samples $x = 0.05$ and 0.1 becomes ferromagnetically ordered (see Fig. 3b, e). So, the value of the AFM order temperatures T_{AFM} for $x = 0.05$ and 0.1 samples are reduced significantly compared to the $x = 0$ sample. However, the AFM state extends down to the base-T unlike in the undoped sample[6]. Figure 3c, f show the temperature dependences of the transverse depolarization rates $\lambda_{T,AFM}$ and $\lambda_{T,FM}$ for the $x = 0.05$ and 0.1 samples for the AFM and the FM components, respectively. In general, muon spin depolarization may arise from the finite width of the static internal field distribution and/or by dynamic spin fluctuations. Due to the small value of the longitudinal relaxation rate λ_L in the present case, the damping is predominantly caused by former effect. The value of $\lambda_{T,AFM}$ is at least a factor of two higher than $\lambda_{T,FM}$, which is similar to the undoped sample, indicating a more disordered nature of the AFM state in Co$_3$Sn$_{2-x}$In$_x$S$_2$. $\lambda_{T,AFM}$ monotonously decreases with increasing temperature, similar to the internal field and becomes zero at T_{AFM}. On the other hand, $\lambda_{T,FM}$ shows increase upon increasing temperature and shows a maximum near the transition temperature T_{FM} with a higher value as compared to the one at 5 K. Such an unconventional temperature evolution of the depolarization rate was also observed in the $x = 0$ sample[6], and implies that the
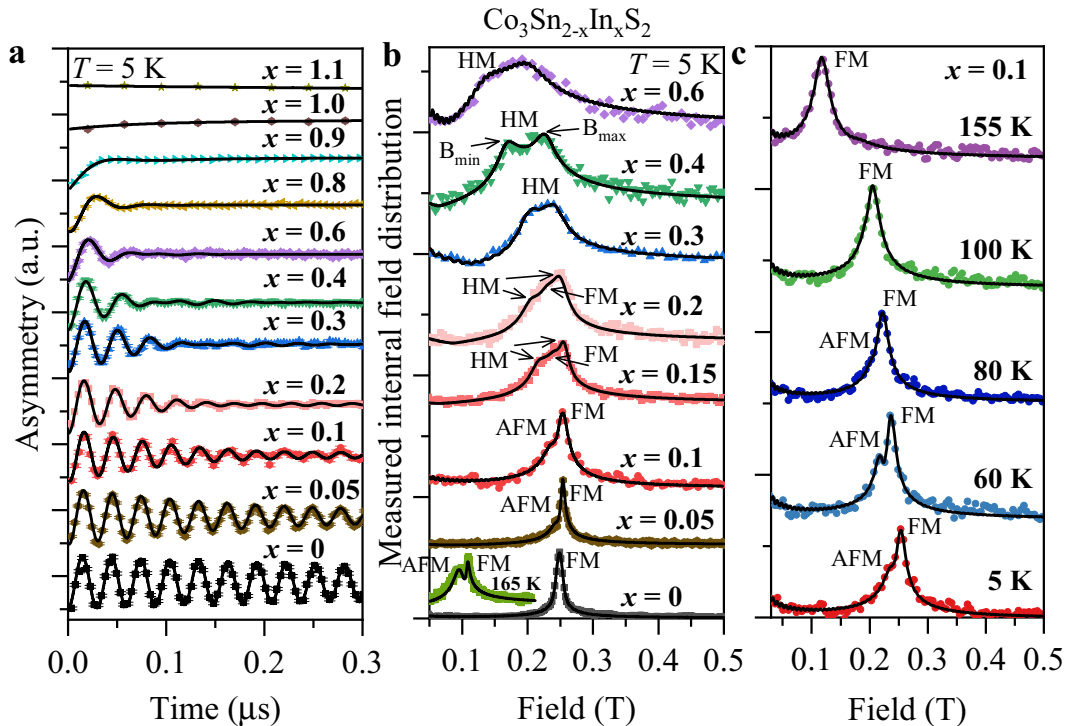
Fig. 2 (Color online) Zero-field (ZF) µSR time spectra for CoSn$_{2-x}$In$_x$S$_2$. Zero-field (ZF) µSR time spectra (**a**) and the corresponding Fourier transform amplitudes (**b**) of the oscillating components for undoped and various In-doped CoSn$_{2-x}$In$_x$S$_2$, recorded at 5 K. FFT amplitude for the $x = 0$ sample, recorded at 165 K, is also shown. The error bars represent the s.d. of the fit parameters. **c** Fourier transform amplitudes of the oscillating components of the µSR time spectra for various temperatures for the $x = 0.1$ sample. FFT amplitudes were normalized to its maximum value to make the signals well visible especially for samples for high In-doping. FM, AFM, and HM denote the out-of-plane ferromagnetic, in-plane antiferromagnetic and helical orders, respectively (see the text for the explanation).

magnetism becomes more disordered upon approaching the transition. The domain wall motion near the critical temperature, as recently reported[39], may explain such a behavior. Figure 4a, b show the temperature dependences of the internal fields for the FM and HM components for $x = 0.15$ and 0.2 samples, respectively. We note that for simplicity we define the internal field in the helical phase $B_{int,Hel}$ as the average value of the minimum and the maximum cutoff fields $B_{int,Hel} = (B_{min} + B_{max})/2$. Both order parameters show a monotonous decrease. Both FM and HM regions exhibit similar transition temperatures. However, the FM fraction is only 30 and 15% for $x = 0.15$ and 0.2 samples, respectively. For $x \geq 0.3$, only HM order is observed. The temperature dependences of the corresponding internal fields $B_{int,Hel}$ and the relaxation rates $\lambda_{T,HM}$ are displayed in Fig. 4d, f, respectively, revealing a gradual increase in the internal field as the temperature is lowered. This suggests a second-order-like behavior of the thermal phase transition and reveals the continuous development of the ordered moment size, as is the case for the undoped sample[6]. The value of $B_{int,Hel}$ at the lowest measured temperature of $T = 2$ K is continuously reduced with In-doping. $B_{int,Hel}$ becomes zero for the semiconducting sample of $x = 1$[19,40]. The temperature dependence of the magnetic volume fraction extracted from the weak-TF data for all measured In-doped samples is displayed in Fig. 4e. Interestingly, the samples with $x \leq 0.9$, in which the long-range magnetism is observed, are fully ordered at low temperatures. The semiconducting sample $x = 1$ shows a significantly reduced ordered volume fraction, which is suppressed nearly to zero for $x = 1.1$. To characterize the changes in magnetic critical temperature, we identify the temperatures T_{FM}, T_{AFM}, and T_{HM} at which the internal fields of the FM, AFM, and HM components start to appear, which coincides with the temperature at which the total magnetic fraction is 50%.

Temperature-doping magnetic phase diagram

The results are summarized in Fig. 5, showing a complex temperature-doping phase diagram for Co$_3$Sn$_{2-x}$In$_x$S$_2$. Figure 5a displays the evolution of the FM, AFM, and HM ordering temperatures as a function of In-content. In our previous work[6], based on the theoretical group analysis and the local field simulations at the muon site, we showed that the $x = 0$ sample exhibits a phase separation between in-plane AFM (Fig. 5d) and out-of-plane FM states (Fig. 5e) in the temperature range between $T_C^* \simeq 90$ K and $T_{AFM} \simeq 172$ K, while below $T_C^* \simeq 90$ K a homogeneous FM structure is observed. Here, we uncover an incommensurate HM phase and in the temperature-doping phase diagram, we identify five different magnetic phases: a ferromagnetic (FM), phase separation between ferromagnetic and antiferromagnetic (FM + AFM), phase separation between ferromagnetic and helimagnetic (FM + HM), helimagnetic (HM), and a paramagnetic phase (PM). The determination of the corresponding transition temperatures is described above. The present experiments suggest that a small amount of In-doping tunes the ground state of the Co$_3$Sn$_{2-x}$In$_x$S$_2$ from FM via a mixed FM + AFM and FM + HM states to a HM structure. The critical In-content at which the transition into an incommensurate HM state takes place is $x_{cr,1} \simeq 0.3$. The suppression of the out-of-plane FM state is also supported by the strong reduction of the c-axis coercive field, extracted from bulk magnetization measurements (Fig. 5c). Small c-axis coercive field for $x \geq 0.3$ also points to the fact that the moments in the HM state are mostly in-plane. Thus, a helical version of the in-plane AFM state is anticipated at the high In-doping region of the phase diagram. It is important to note that there is a volume wise competition between FM and AFM/HM states, meaning that the FM volume fraction is heavily reduced upon approaching $x_{cr,1}$ (Fig. 5b), while the ordered moment size (Fig. 5b) is only slightly reduced between $x = 0$ and 0.2 and is
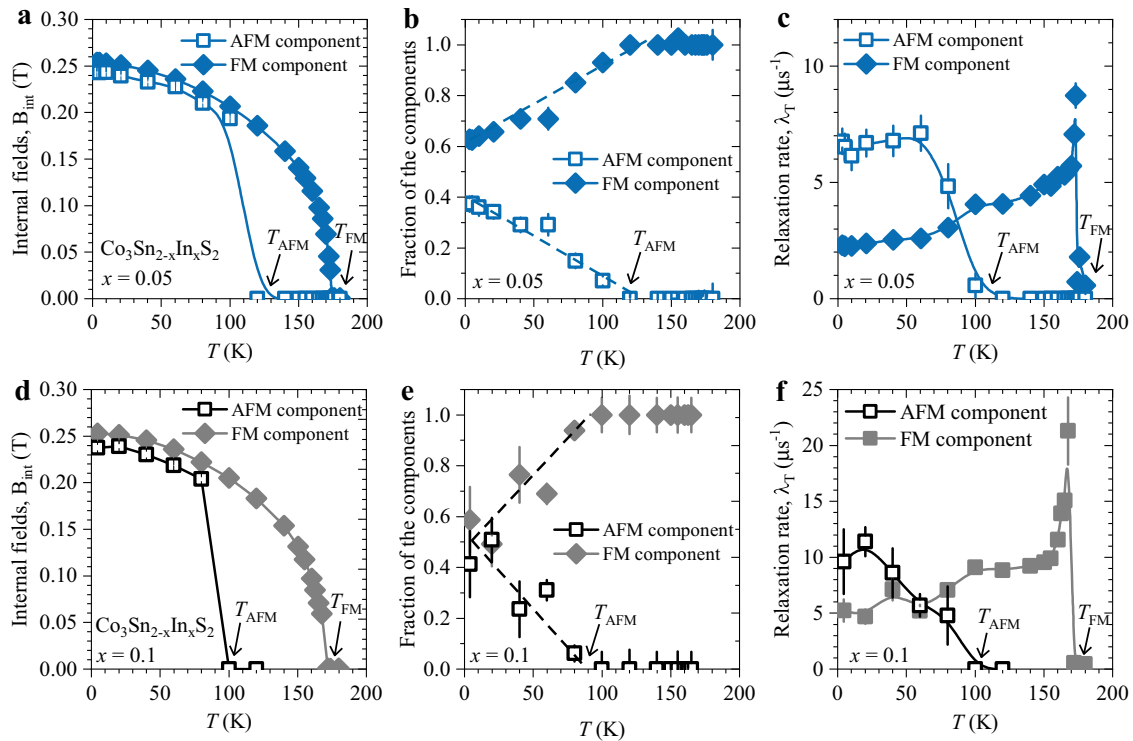
Fig. 3 (Color online) The temperature dependence of various fit parameters of the μSR experiments. The temperature dependences of the internal magnetic fields (**a**, **d**), the relative volume fractions (**b**, **e**) and the transverse relaxation rates (**c**, **f**) of the two magnetically ordered regions in the samples $x = 0.05$ and 0.1. The error bars represent the s.d. of the fit parameters. Arrows mark the critical temperatures T_{AFM} and T_{FM} for AFM and FM components.

abruptly suppressed at $x_{cr,1}$. This demonstrates that the change from FM to HM happens through a first order transition. Upon further increasing the In-content, the HM ordering temperature T_{Hel} gradually decreases and is suppressed towards the critical doping $x_{cr,2} \simeq 1$, at which the system exhibits a metal to semiconductor transition (see the Supplementary Fig. 3 and the Supplementary Note 2). Indium doping also causes a smooth reduction of the internal field $B_{int,Hel}$, i.e. the ordered moment size of the HM state, to zero at $x_{cr,2} \simeq 1$ (Fig. 5b), suggesting a continuous QPT across $x_{cr,2}$. Moreover, the magnetically ordered fraction V_m is unchanged as the In-content is increased from 0 to 0.9, indicating a fully ordered volume for all samples, exhibiting long-range magnetic order. V_m is reduced drastically for $x_{cr,2} \simeq 1$. For $x = 1.1$, V_m approaches nearly zero. The continuous suppression of the ordered moment size and the sharp reduction of V_m from 1 to ~0 across $x_{cr,2}$ classiffies the transition from long-range magnetic metal to a paramagnetic semiconductor as a second-order quantum phase transition. This provides the direct evidence of a QCP at $x_{cr,2}$ in $Co_3Sn_{2-x}In_xS_2$. This is to the best of our knowledge the first microscopic experimental observation of a QCP in a topological kagome magnet. The presence of the QCP in $Co_3Sn_{2-x}In_xS_2$ suggests that the physical properties of this material at low temperatures are controlled by the QCP. Our high pressure μSR measurements (see the details in the Supplementary Fig. 4 and the Supplementary Note 3) show strong and unusual reduction of the pressure induced suppression rate of the magnetic ordering temperature for the sample $x = 0.9$ as compared to the suppression rate for the samples $x \leq 0.8$, which might also be related to the proximity of the $x = 0.9$ sample to the putative quantum critical point at $x \simeq 1$. The presence of small dynamic magnetic regions in the $x = 1$ sample may also be linked to the QCP.

DISCUSSION

According to our previous experiments and DFT calculations[6] the out-of-plane ferromagnetic interactions and in-plane antiferro-magnetic interactions within the kagome plane of $Co_3Sn_2S_2$ have similar energy scales. The HM structure in this system may be interpreted by a competition between dominant Heisenberg-type (FM and AFM) interactions and a weaker antisymmetric Dzyaloshinskii–Moriya (DM) interaction. It seems that In-doping affects the competing interactions such that it promotes the HM state. We note that hydrostatic pressure also causes a suppression of both FM and AFM states[41], but a pressure as high as 20 GPa is needed at which both orders are suppressed simultaneously. No HM phase was induced by pressure. In $Co_3Sn_{2-x}In_xS_2$ however, only a small amount of In is sufficient to push the system towards the HM state. Indium substitution introduces holes to the system and at the same time increases the separation of the kagome layers, while hydrostatic pressure shrinks the lattice and no doping is expected. This suggests that lattice expansion and/or hole doping disfavors the out-of-plane FM state, and leads to an incommensurate HM state. The present μSR experiments along with the AHC and c-axis magnetic hysteresis measurements suggest the in-plane HM state (moments rotate within the ab-plane, see the discussion below) for $x \geq 0.3$. A helical variation of the in-plane AFM structure (see Fig. 5e) is possible. However, additional experiments such as polarized neutron scattering is necessary to determine the precise nature of this magnetic phase. The advantage of μSR is its extreme sensitivity to low-moment magnetism as it is the case for $Co_3Sn_2S_2$.

It is well established that the system $Co_3Sn_2S_2$ has a large Berry curvature driven anomalous Hall conductivity (AHC) $\sigma_{xy,int}$[20]. Recently, it was shown that $\sigma_{xy,int}$ features a maximum at $x \simeq$ 0.15 above which it sharply decreases and becomes negligibly small for $x \geq 0.3$, well below the magnetic to paramagnetic critical
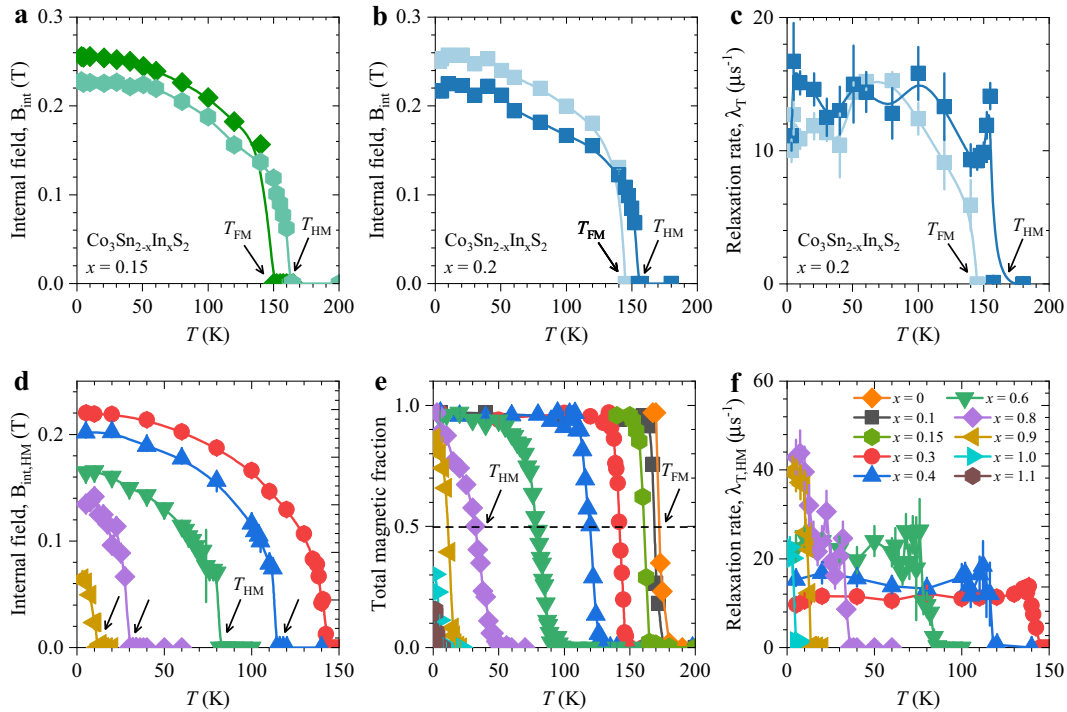
Fig. 4 (Color online) The temperature dependence of various fit parameters of the μSR experiments. The temperature dependences of the internal magnetic fields of the two magnetically ordered regions in the samples $x = 0.15$ (**a**) and 0.2 (**b**). **c** The temperature dependence of the transverse relaxation rates of the two magnetically ordered regions in the sample $x = 0.2$. Arrows mark the critical temperatures T_{FM} and T_{Hel} for FM and helical magnetic components, respectively. The temperature dependences of the average value of magnetic fields (**d**) and the transverse relaxation rates (**f**) for the helical magnetic component shown for various In-doped samples. **e** The temperature dependence of the total magnetic volume fraction for various In-doped samples. The error bars represent the s.d. of the fit parameters. Arrows in **e** mark the temperature at which the magnetic fraction is 50%.

doping $x_{cr,2} \simeq 1$. This indicates that the doping induced disappearance of the $\sigma_{xy,int}$ is closely related to the depression of the FM state and that around the critical doping $x_{cr,1} \simeq 0.3$, both the ferromagnetism and the AHE are strongly suppressed simultaneously. This can be understood by the DFT calculations, showing that the c-axis FM order has the dominant contribution into the AHC[6] (see the Supplementary Fig. 5 and the Supplementary note 4). Thus, the data provide direct experimental evidence for the quantum tuning (In-doping) of topological Hall conductivity driven by the competition between the FM, AFM, and HM structures in the kagome lattice. It is remarkable that the phase diagram (Fig. 5a) exhibits a doping region where different magnetically ordered phases, each of which may possess distinct topological responses, coexist at zero temperature. The non-zero but small value of $\sigma_{xy,int}$ and the coercive field for $x \geq 0.3$ (Fig. 5c) may indicate, either the presence of an experimentally non-resolvable small FM fraction in these high In-doped samples or the presence of some canting within the in-plane HM structure, giving rise to a small c-axis net FM moment and a related AHC component. Note that the AHC in the undoped system scales with the FM volume fraction as a function of temperature[6]. Since the FM fraction is gradually reduced by In-doping, one would expect the gradual suppression of $\sigma_{xy,int}$ as well. Instead, we see a sharp peak of $\sigma_{xy,int}$ at $x \simeq 0.15$. We currently do not provide a microscopic mechanism explaining this effect. However, we discuss several possible reasons for this behavior: (1) According to first principle calculations, the anomalous Hall conductivity $\sigma_{xy,int}$ strongly depends on the electron density n_e (which does not change much with temperature). In-doping causes the reduction of the FM fraction, but it may modify n_e in the FM volumes of the sample in such a way that σ_{xy} increases. Once the FM fraction becomes negligible, $\sigma_{xy,int}$ also becomes negligibly small. (2) The maximum of $\sigma_{xy,int}$ occurs in the doping range where FM and HM

regions coexist. Accordingly, a possible electron/hole transfer between FM and HM phases appears possible, thereby providing a higher effective doping for the FM region and therefore contributing to the increase of the $\sigma_{xy,int}$. (3) Indium doping might modify the band structure leading to an enhancement of $\sigma_{xy,int}$. The detailed electronic structure for this system $Co_3Sn_{2-x}In_xS_2$, considering here provided magnetic phase diagram, should be done and this is a subject of the separate studies.

In summary, the transition metal based kagome material $Co_3Sn_{2-x}In_xS_2$ is an ideal platform to study two intriguing, and in this case intertwined, properties of quantum materials, namely magnetism and topological electronic band structure. Our key finding is the possibility of an effective quantum tuning of the competition between FM, in-plane AFM and mostly in-plane HM orders within the kagome plane of $Co_3Sn_{2-x}In_xS_2$ by In-doping and the presence of multiple quantum phase transitions of different nature in the phase diagram of this system. Our experiments show the presence of at least two zero temperature phase transitions in the phase diagram of this system. One at the low In-doping of $x_{cr,1} \simeq 0.3$, where a QPT from a FM to a HM state through mixed states is observed and a second one at $x_{cr,2} \simeq 1$, with a transition from a helical metallic to a paramagnetic semiconducting state. Remarkably, the QPT from FM to incommensurate HM state is first order, while the transition from HM metal to a PM semiconductor is a continuous/second-order transition. Thus, we have uncovered a quantum critical point (QCP) in $Co_3Sn_{2-x}In_xS_2$ at the doping level of $x_{cr,2} \simeq 1$. The interplay between the competing magnetic states, the charge carrier density within the FM regions and the spin–orbit coupled band structure further seem to induce non-trivial variations of the topological properties of $Co_3Sn_{2-x}In_xS_2$. This is evidenced by a non-monotonous In-doping dependence of the anomalous Hall conductivity with the nearly full suppression of $\sigma_{xy,int}$ above
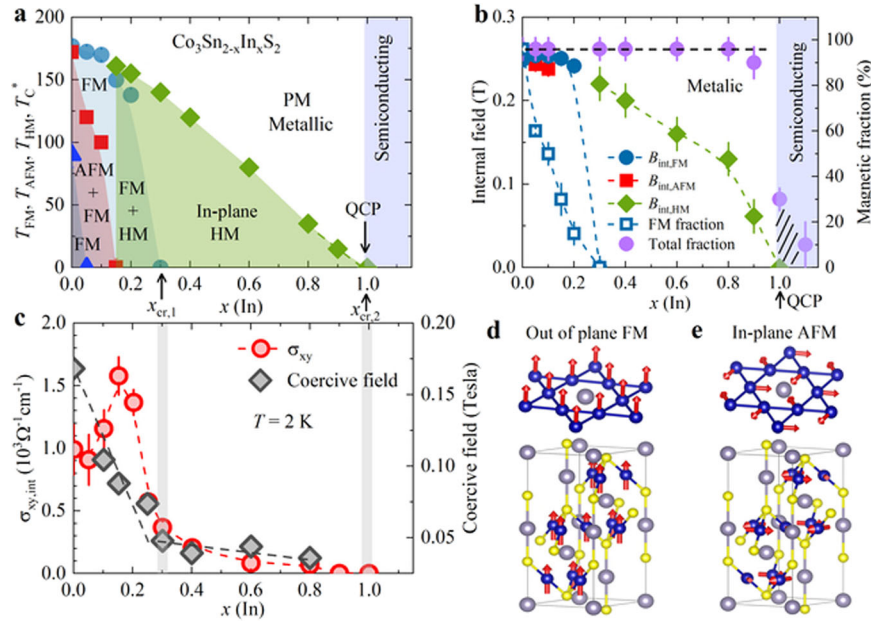
Fig. 5 (Color online) Phase diagrams for CoSn$_{2-x}$In$_x$S$_2$. a Temperature-doping phase diagram. T_{FM}, T_{AFM} and T_{HM} indicates the FM, AFM, and putative HM transition temperatures. T_C^* denotes the temperature below which only the FM state exists. **b** The doping dependence of the base-temperature value of the internal internal magnetic fields, the FM ordered fraction and the total magnetic fraction. The black dashed line marks the region with weak disordered magnetic response. **c** The In-doping dependence of the in-plane anomalous Hall conductivity $\sigma_{xy,int}$ and the coercive field at $T = 2$ K. **d, e** Spin structures of Co$_3$Sn$_2$S$_2$, i.e., the c-axis aligned FM structure (R-3m' subgroup) and the in-plane AFM structure (R-3m subgroup). HM state is most likely a helical variation of the in-plane AFM structure.

$x_{cr,1} \simeq 0.3$, where the FM state disappears. Therefore the exciting perspective arises of a magnetic system in which the topological response can be controlled, and thus explored, over a wide range of parameters.

METHODS

Homogeneous macroscopic crystal structure
The crystal structure of the samples Co$_3$Sn$_{2-x}$In$_x$S$_2$ was examined by powder X-ray diffraction measurements, revealing a homogeneous rhombohedral macroscopic lattice structure. The obtained lattice parameters a and c show smooth linear dependence on the In-content x, as shown in our previous work[19]. Thus, we do not see any lattice irregularities or distortions on the macroscopic scale.

µSR experiment
Positive muons μ^+, which are 100% spin-polarized when generated, are implanted one at a time in the sample. Thermalization of the positively charged μ^+ at interstitial lattice sites occurs almost instanteously. They then can be used as magnetic microprobes, precessing around the local B_μ field felt at their stopping site. They precess with the Larmor frequency $\omega = 2\pi\nu_\mu = \gamma_\mu/(2\pi)B_\mu$ (muon gyromagnetic ratio $\gamma_\mu/(2\pi) = 135.5$ MHz T^{-1}).

Single crystals of Co$_3$Sn$_{2-x}$In$_x$S$_2$ were studied at ambient pressure with the GPS (πM3 beamline)[42] and the HAL-9500 (πE3 beamline) µSR instruments at the Paul Scherrer Institute, Switzerland. High-momentum ($p_\mu = 100$ MeV/c) beam of muons (µE1 beamline) is used to investigate the $x = 0.8$ and 0.9 crystals as a function of hydrostatic pressure.

Analysis of weak TF-µSR data
The following function is used to analyze[43] the asymmetry spectra collected in the weak TF setup:

$$A_S(t) = A_p \exp(-\lambda t) \cos(\omega t + \phi). \tag{1}$$

Here, $A(t)$ and A_p is the time-dependent asymmetry and the amplitude of the oscillation, respectively. A_p is measure of the paramagnetic volume fraction. λ is the muon spin depolarization rate, arising from the paramagnetic spin fluctuations and/or nuclear dipolar moments. ω and ϕ is the Larmor precession frequency and a phase offset, respectively.
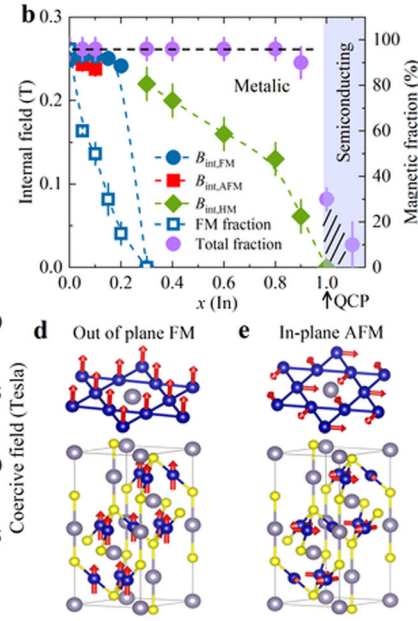
When refining $A(t)$, the zero was allowed to vary for each temperature in order to account for the asymmetry baseline shift occurring for magnetically ordered samples. The magnetically ordered volume fraction is then obtained at each temperature T by $1 - A_p(T)/A_p(T_{max})$, where $A_p(T_{max})$ is the amplitude of the paramagnetic phase at high temperature.

Analysis of ZF-µSR data
The ZF-µSR spectra for $x < 0.3$ were analyzed using the following commensurate model:

$$A_{ZF}(t) = F\left(\sum_{j=1}^{2}\left(f_j \cos(2\pi\nu_j t + \phi)e^{-\lambda_j t}\right) + f_L e^{-\lambda_L t}\right)$$
$$+ (1-F)\left(\frac{1}{3} + \frac{2}{3}\left(1 - (\sigma t)^2\right)e^{-\frac{1}{2}(\sigma t)^2}\right). \tag{2}$$

The model in (2) is composed of two components: a slowly relaxing "longitudinal" component, and an anisotropic magnetic contribution with an oscillating "transverse" component. The longitudinal component is the result of a local field component experienced by the muon that is parallel to the initial muon spin polarization. This results in the so-called "one-third tail" with $f_L = \frac{1}{3}$ due to the orientational averaging of the randomly oriented fields in polycrystalline samples. As the orientation between field and polarization changes from being perpendicular to parallel, f_L varies between zero and unity for single crystalline samples. It is important to note that the whole volume of the sample is magnetically ordered nearly up to T_C. Only very close to the transition there is a paramagnetic component in addition to the magnetically ordered contribution. This is characterized by the width σ of the field distribution at the muon site created by the densely distributed nuclear moments. The temperature-dependent magnetic ordering fraction $0 \leq F \leq 1$ governs the trade-off between magnetically-ordered and paramagnetic behaviors.

The field distribution for the samples $x \geq 0.3$ presented in Fig. 2b is characterized by a minimum (B_{min}) and a maximum (B_{max}) cutoff field, which is consistent with the incommensurate helimagnetic order, and is well described by the field distribution given by[34–38]:

$$P(B) = \frac{2}{\pi} \frac{B}{\sqrt{(B^2 - B_{min}^2)(B_{max}^2 - B^2)}} \tag{3}$$

Analysis of ZF-μSR data under pressure

Since the large fraction (~50%) of the μSR signal originates from muons landing in the MP35N pressure cell, the data were modeled by weighted sum of a contribution of the sample and a contribution of the pressure cell:

$$A(t) = A_S(0)P_S(t) + A_{PC}(0)P_{PC}(t), \qquad (4)$$

where $A_S(0)$ and $A_{PC}(0)$ are the initial asymmetries and $P_S(t)$ and $P_{PC}(t)$ are the time-dependent muon-spin polarizations of the muons stopping in the sample and the pressure cell, respectively. A damped Kubo–Toyabe function[33,44] was used to analyze the signal of the pressure cell.

Pressure cell

Similar to previous studies[44,45], hydrostatic pressures up to 1.9 GPa were generated in a double wall clamp cell made of CuBe/MP35N material[44–46] and by using Daphne oil as a pressure transmitting medium. The precise value of the applied pressure was obtained by following the superconducting transition of an indium plate by AC susceptibility.

DATA AVAILABILITY

All relevant data are available from the authors. Alternatively, the data can be accessed through the link http://musruser.psi.ch/cgi-bin/SearchDB.cgi with the following details: HAL-Year 2019 and run title Co3SnInS. GPS-Year 2019 and run title CSS. GPD-Year 2019 and run title CSS. GPS-Year 2020 and run title CSS.

REFERENCES

1. Keimer, B. & Moore, J. E. The physics of quantum materials. *Nat. Phys.* **13**, 1045–1055 (2017).
2. Wang, J. & Zhang, S.-C. Topological states of condensed matter. *Nat. Mater.* **16**, 1062–1067 (2017).
3. Hasan, M. Z. & Kane, C. L. Topological insulators. *Rev. Mod. Phys.* **82**, 3045–3067 (2010).
4. Wen, X. G. Colloquium: Zoo of quantum-topological phases of matter. *Rev. Mod. Phys.* **89**, 041004 (2018).
5. Yin, J.-X. et al. Giant and anisotropic spin-orbit tunability in a strongly correlated kagome magnet. *Nature* **562**, 91–95 (2018).
6. Guguchia, Z. et al. Tunable anomalous Hall conductivity through volume-wise magnetic competition in a topological kagome magnet. *Nat. Commun.* **11**, 559 (2020).
7. Ghimire, N. J. & Mazin, I. I. Topology and correlations on the kagome lattice. *Nat. Mater.* **19**, 137–138 (2020).
8. Ye, L. et al. Massive Dirac fermions in a ferromagnetic kagome metal. *Nature* **555**, 638–642 (2018).
9. Han, T.-H. et al. Fractionalized excitations in the spin-liquid state of a kagome-lattice antiferromagnet. *Nature* **492**, 406–410 (2012).
10. Yin, J.-X. et al. Negative flatband magnetism in a spin-orbit coupled kagome magnet. *Nat. Phys.* **15**, 443–448 (2019).
11. Legendre, J. & Hur, K. L. Magnetic topological kagome systems. *Phys. Rev. Res.* **2**, 022043(R) (2020).
12. Ghimire, N. J. et al. Competing magnetic phases and fluctuation-driven scalar spin chirality in the kagome metal YMn$_6$Sn$_6$. *Sci. Adv.* **6**, eabe2680 (2020).
13. Guguchia, Z. et al. Nodeless kagome superconductivity in LaRu$_3$Si$_2$. *Phys. Rev. Mater.* **5**, 034803 (2021).
14. Jiang, Y. -X. et al. Discovery of topological charge order in kagome superconductor KV$_3$Sb$_5$. Preprint at https://arxiv.org/abs/2012.15709 (2021).
15. Weihrich, R., Pöttgen, R. & Pielnhofer, F. From laboratory press to spins with giant effects. *Angew. Chem.* **130**, 15868–15870 (2018).
16. Weihrich, R., Anusca, I. & Zabel, M. Half-antiperovskites: structure and type-antitype relations of Shandites M$_{3/2}$As (M = Co, Ni; A = In, Sn). *Z. Anorg. Allg. Chem.* **631**, 1463–1470 (2005).
17. Weihrich, R. & Anusca, I. Half antiperovskites. III—Crystallographic and electronic structure effects in Sn$_{2−x}$In$_x$Co$_3$S$_2$. *Z. Anorg. Allg. Chem.* **632**, 1531–1537 (2006).
18. Schnelle, W. et al. Ferromagnetic ordering and half-metallic state of Sn$_2$Co$_3$S$_2$ with the Shandite-type structure. *Phys. Rev. B* **88**, 144404 (2013).
19. Zhou, H. et al. Enhanced anomalous Hall effect in magnetic topological semi-metal Co$_3$Sn$_{2−x}$In$_x$S$_2$. *Phys. Rev. B* **101**, 125121 (2020).
20. Liu, E. et al. Giant anomalous Hall effect in a ferromagnetic kagome-lattice semimetal. *Nat. Phys.* **14**, 1125–1131 (2018).
21. Muechler, L., Liu, E., Xu, Q., Felser, C. & Sun, Y. Emerging chiral edge states from the confinement of a magnetic Weyl semimetal in Co$_3$Sn$_2$S$_2$. *Phys. Rev. B* **101**, 115106 (2020).
22. Wang, Q. et al. Large intrinsic anomalous Hall effect in half-metallic ferromagnet Co$_3$Sn$_2$S$_2$ with magnetic Weyl fermions. *Nat. Commun.* **9**, 3681 (2018).
23. Xu, Q. et al. Topological surface Fermi arcs in magnetic Weyl semimetal Co$_3$Sn$_2$S$_2$. *Phys. Rev. B* **97**, 235416 (2018).
24. Belopolski, I. et al. Signatures of a topological Weyl loop in Co$_3$Sn$_2$S$_2$. Preprint at https://arxiv.org/abs/2005.02400 (2020).
25. Lachman, E. et al. Exchange biased anomalous Hall effect driven by frustration in a magnetic kagome lattice. *Nat. Commun.* **11**, 560 (2020).
26. Kassem, M. A. Novel magnetic and electronic properties of kagomé-lattice cobalt-shandites. Ph.D. thesis (Kyoto University) (2017).
27. Sachdev, S. Kagome- and triangular-lattice Heisenberg antiferromagnets: ordering from quantum fluctuations and quantum-disordered ground states with unconfined bosonic spinons. *Phys. Rev. B* **45**, 12377 (1992).
28. Chubukov, A. First-order transition in frustrated quantum antiferromagnets. *Phys. Rev. B* **44**, 392 (1991).
29. Guguchia, Z. et al. Probing the quantum phase transition in Mott insulator BaCoS$_2$ tuned by pressure and Ni-substitution. *Phys. Rev. Mater.* **3**, 045001 (2019).
30. Frandsen, B. A. et al. Volume-wise destruction of the antiferromagnetic Mott insulating state through quantum tuning. *Nat. Commun.* **7**, 12519 (2016).
31. Uemura, Y. J. et al. Phase separation and suppression of critical dynamics at quantum phase transitions of MnSi and (Sr$_{1−x}$Ca$_x$)RuO$_3$. *Nat. Phys.* **3**, 29–35 (2007).
32. Goko, T. et al. Restoration of quantum critical behavior by disorder in pressure-tuned (Mn,Fe)Si. *npj Quantum Mater.* **2**, 44 (2017).
33. Kubo, R. & Toyabe, T. *Magnetic resonance and relaxation.* (North Holland, 1967).
34. Amato, A. et al. Understanding the μSR spectra of MnSi without magnetic polarons. *Phys. Rev. B* **89**, 184425 (2014).
35. Schenck, A., Andreica, D., Gygax, F. N. & Ott, H. R. Extreme quantum behavior of positive muons in CeAl$_2$ below 1 K. *Phys. Rev. B* **65**, 024444 (2001).
36. Yaouanc, A. Dual nature of magnetism in MnSi. *Phys. Rev. Res.* **2**, 013029 (2020).
37. Khasanov, R. et al. High-pressure magnetic state of MnP probed by means of muon-spin rotation. *Phys. Rev. B* **93**, 180509(R) (2016).
38. Khasanov, R. et al. Magnetic states of MnP: muon-spin rotation studies. *J. Phys.* **29**, 164003 (2017).
39. Howlader, S., Ramachandran, R., Yogesh Singh, S. & Sheet, G. Domain structure evolution in the ferromagnetic Kagome-lattice Weyl semimetal Co$_3$Sn$_2$S$_2$. *J. Phys.* **33**, 075801 (2021).
40. Pielnhofer, F. et al. Half antiperovskites VI: on the substitution effects in Shandites Sn$_{2−x}$In$_x$Co$_3$S$_2$. *Z. Anorg. Allg. Chem.* **640**, 286–294 (2014).
41. Chen, X. et al. Pressure-tunable large anomalous Hall effect of the ferromagnetic Kagome-lattice Weyl semimetal Co$_3$Sn$_2$S$_2$. *Phys. Rev. B* **100**, 165145 (2019).
42. Amato, A. et al. The new versatile general purpose surface-muon instrument (GPS) based on silicon photomultipliers for μSR measurements on a continuous-wave beam. *Rev. Sci. Instrum.* **88**, 093301 (2017).
43. Suter, A. & Wojek, B. M. Musrfit: a free platform-independent framework for μSR data analysis. *Phys. Procedia* **30**, 69–73 (2012).
44. Guguchia, Z. et al. Direct evidence for the emergence of a pressure induced nodal superconducting gap in the iron-based superconductor Ba$_{0.65}$Rb$_{0.35}$Fe$_2$As$_2$. *Nat. Commun.* **6**, 8863 (2015).
45. Khasanov, R. et al. High pressure research using muons at the Paul Scherrer Institute. *High. Press. Res.* **36**, 140–166 (2016).
46. Andreica, D. Ph.D. thesis (IPP/ETH-Zürich, 2001). Magnetic phase diagram in some Kondo-lattice compounds: microscopic and macroscopic studies.

AUTHOR CONTRIBUTIONS

Z.G. conceived the study. μSR experiments and corresponding discussions: Z.G., C.N.W., C.M.III., R.K., A.A., I.B., T.A.C., J.-X.Y., S.-S.Z., M.Z.H. and H.L. μSR data analysis: Z.G.

Growth of single crystals and transport measurements: H.Z. and S.J. Band structure and AHC calculations: S.S.T. and T.N. Figure development and writing the paper: Z.G. with contributions from all authors. All authors discussed the results, interpretation, and conclusion.

COMPETING INTERESTS

The authors declare no competing interests.

ADDITIONAL INFORMATION

Supplementary information The online version contains supplementary material available at https://doi.org/10.1038/s41535-021-00352-3.

Correspondence and requests for materials should be addressed to Z.G.

Reprints and permission information is available at http://www.nature.com/reprints